Article

Not peer-reviewed version

Rotating Photodisc Reactor (RPR) Used in The Photodegradation of Pyridine Using Zinc Oxide as a Catalyst Doped with Aluminum Nanoparticles Irradiated with Natural Light

Carlos Montalvo Romero * , Claudia Alejandra Aguilar-Ucán , Edith Lemus , Rosa María Cerón-Bretón , Julia Griselda Ceron-Breton , Juan Carlos Robles Heredia , Alejandro Ruiz Marin

Posted Date: 9 October 2024

doi: 10.20944/preprints202410.0598.v1

Keywords: Pyridine; rotating photodisc reactor (RPR); zinc oxide; aluminum

Article

Rotating Photodisc Reactor (RPR) Used in The Photodegradation of Pyridine Using Zinc Oxide as a Catalyst Doped with Aluminum Nanoparticles Irradiated with Natural Light

Montalvo Romero Carlos, Lemus Jauregui Edith, Aguilar Ucan Claudia A., Ceron Breton Rosa M., Ceron Breton Julia G., Robles Heredia Juan C. and Ruiz Marín Alejandro

Autonomous University of Carmen. 56th Street #4, Benito Juarez Colony, Zip Code 24180. Ciudad del Carmen, Campeche, Mexico

* Correspondence: c_montalvo10@hotmail.com

Abstract: Pyridine was degraded in a rotating photodisc reactor (RPR) using zinc oxide (ZnO) doped with aluminum nanoparticles (ZnO-Al) as a catalyst and natural light lamps. The reactor disks, made of clay, have a surface area of 329.7209 m². The reactor was operated as a semi-batch system, handling a volume of 14.8 L and a hydraulic residence time (HRT) of 72 hours at 54 rpm with a constant flow rate. The results indicated an average degradation of 50.6% after an HRT of 72 hours, with a maximum degradation of 62%. Characterization results confirmed the effectiveness of the doping process, showing an aluminum concentration of 4.11% by mass in the catalyst, as determined by X-ray techniques. Overall, the doping process proved effective for the zinc oxide catalyst, as evidenced by a reduction in the catalyst bandgap from 3.37 eV for undoped ZnO to 3.08 eV for the doped version, making it sufficiently active under natural light.

Keywords: pyridine; rotating photodisc reactor (RPR); zinc oxide; aluminum

Introduction

Industrial development has grown significantly in recent years, leading to a substantial increase in industrial waste discharge into receiving bodies of water. This has resulted in the release of various pollutants into water bodies. Numerous persistent organic compounds have been identified, including phenols, chlorophenols, and pyridine, which are compounds commonly associated with industrial activities (Koe et al., 2020).

Pyridine is widely used in the synthesis of various compounds, including fertilizers, paints, and pesticides. Advanced oxidation processes are an effective alternative for degrading persistent organic compounds. These processes include non-photocatalytic methods such as ultrasound as well as photocatalytic methods such as heterogeneous photocatalysis.

The increasingly acceptable use of chemical products in industries and homes has led to an increase in organic pollutants in effluents (Careghini et al., 2015).

Various industries release a significant number of aromatic compounds into the environment due to their widespread use in many industries. Among these, heterocyclic aromatic compounds such as pyridine and its derivatives are of particular concern as environmental pollutants due to their recalcitrant, toxic, and teratogenic nature (Santhi et al., 2015; Bello and Raman, 2018).

Pyridine and substituted pyridines are important intermediates for the synthesis of pharmaceuticals, herbicides, metal corrosion inhibitors, rubber vulcanization accelerators, etc. (Grigor'eva et al., 2015., Ashok et al., 2022., Frolov and Vereshchagin, 2023., Marinescu and Popa C. (2022). Moctezuma, López, and Zermeño 2016)

Pyridine is produced from coal tar and as a by-product of coal gasification. However, the increased demand for pyridine resulted in the development of cheaper synthesis methods from

 doi:10.20944/preprints202410.0598.v1

acetaldehyde and ammonia, and more than 20,000 tons are manufactured per year worldwide. Therefore, researchers have long sought to develop effective and economically viable techniques to clean the atmosphere of wastes such as pyridine (Elsayed, 2013).

Pyridine, whose chemical formula is C_3H_5N, has become a severe pollution problem due to its extensive use in different branches of industry. Its presence in wastewater is evidenced by an unpleasant odor, which is perceptible at very low concentrations (0.3 μg/L). It also gives water an unpleasant taste, starting at concentrations of 0.82 mg/L. (Aguilar et al., 2012., Song, Chen and Song, 2021, Moctezuma, López and Zermeño 2016; Swarnakar et al. 2013).

ZnO is an important semiconductor material which has a wide range of applications, including transparent conducting oxides, UV light absorbers, and photocatalysis.

Since the band gap energy of ZnO crystals is about 3.3 eV, ZnO can absorb UV rays with wavelengths under 375 nm. Therefore, ZnO has been regarded as an excellent UV shielding material, with broad UV absorption characteristics and photofastness compared with other organic and inorganic UV shielding materials.

The absorbed UV rays excite the valence electrons to the conduction band. When these photo-excited electrons and holes move to the particle surfaces where water and oxygen molecules reside, highly active free radicals such as superoxide anion ($\bullet O_2$) and $\bullet OH$ radical are generated and undergo secondary reactions such as the decomposition of organic compounds.

Mechanism of zinc oxide:

$ZnO \xrightarrow{hv} e^- + h^+$….. (1)

$e^- + h^+ \rightarrow$ recombinación……(2)

$h^+ + H_2O \rightarrow HO\cdot + H^+$…..(3)

$h^+ + HO^+ \rightarrow HO\cdot$ …..(4)

$h^+ + D \rightarrow D^+$(Oxidación directa de compuestos orgánicos …..(5)

$HO\cdot + D \rightarrow D_{oxidado}$(Oxidación de compuestos organicos por radicales $HO\cdot$)…..(6)

$e^- + O_2 \rightarrow O_2^{\cdot -}$ …..(6)

$O_2^{\cdot -} + HO_2\cdot + H^- \rightarrow H_2O_2 + O_2$ …..(7)

$H_2O_2 + e^- \rightarrow HO^- + HO\cdot$ …..(8)

Transition metal doping and mixed oxide formation are two widely studied mechanisms to improve the intrinsic properties of binary oxides. Both procedures have been instrumental in the spectacular increase in applications based on zinc oxide (ZnO) and titanium oxide (TiO_2) thin films (Bozena and Rubinowska, 2013).

Applications derived from metal-doped ZnO in optoelectronic devices include photovoltaic solar cells, flat panel displays, photodetectors, gas sensors, and light-emitting diodes. Most previous works on doped ZnO films focus on doping with group III elements, and in particular, trivalent cations of the elements Al, Ga, and I have been frequently used to enhance the n-type conductivity of ZnO films (Kumar et al. 2017; El Nemr et al., 2019).

Preparing doped material is also a competent method for regulating the surface states of ZnO energy levels, which can be further advanced by changing the doping concentration of semiconductor materials.

As one of the most interesting p-type magnetic doping materials, cobalt-oxide nanostructures are also recognized as attractive materials with broad applications in various fields, such as doping, catalysts, solid-state sensors, and electrochemical devices (Mohammed et al., 2013).

Doping of impurities to create chemical and, in some cases, physical defects in the crystal lattice that would act as the capture and recombination sites of excitons, transition metal (M) atoms are introduced as impurities in ZnO crystallites to tailor the photocatalytic property (Islam et al., 2018).

Methodology

Reagents and Chemicals

Aldrich brand Al_2O_3 oxide with 99.9% purity and Aldrich brand ZnO were used. For pH adjustment, Aldrich brand pyridine, sulfuric acid, and sodium hydroxide solutions were used.

 doi:10.20944/preprints202410.0598.v1

Analytical Methods

Rotating Photo Disk Reactor (RFR)

For the degradation of pyridine, a rotating photo disk reactor (RFR) was used, which consists of 4 stages with 2 disks each. The RFR has a total capacity of 14.8 L and, for each stage, a capacity of 3.7 L; it has a tubular structure support of 0.58 m wide by 1 m high and 1.35 m long. Each stage has an exit at the bottom of the reactor for sampling.

The RFR is a semi-cylindrical fiberglass tub with a height of 0.31 meters and a radius of 0.17 meters. Inside the tub, three fiberglass bulkheads divide the reactor into separate stages. The reactor cover is made of stainless steel and measures 0.30 meters wide by 0.60 meters long. Mounted on the cover are three 15-watt white light lamps strategically positioned to illuminate each stage, as illustrated in Figure 1.

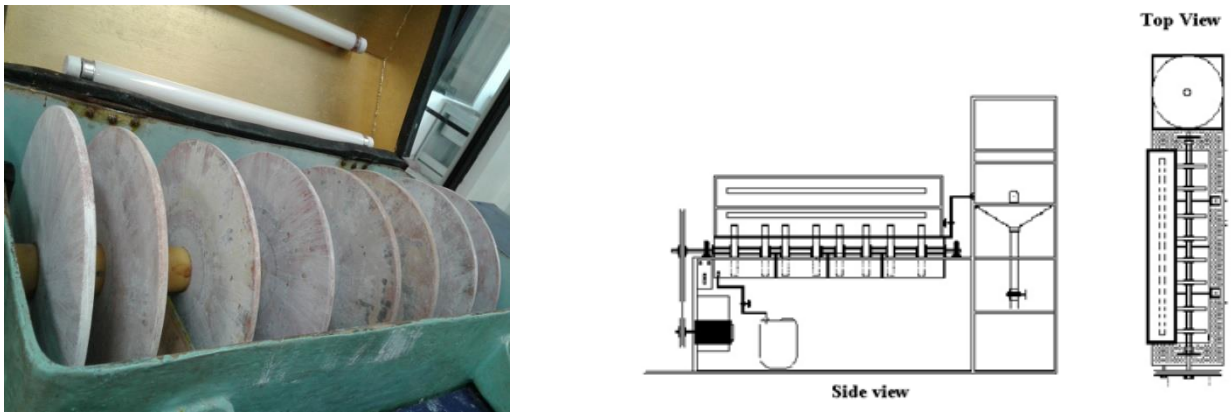

Figure 1. Schematic of the rotating photo disk reactor (RFR).

The RFR disks are moved by a series of pulleys connected to a stainless-steel shaft, which achieves a speed of 55 rpm. This system works with a Dayton brand motor of 1/8 hp, 115 W, with a capacity of 1075 rpm and 1.9 Amps.

The reactor disks, which had a diameter of 0.23 m and a thickness of 0.008 m, were impregnated with zinc oxide and doped with Al^{+3} metallic nanoparticles. The reactor characteristics are summarized in Table 1.

Table 1. Characteristics of the Rotating Photo disk Reactor (RFR).

Number of stages	4
Number of disks per stage	2
Disk diameter	0.23 m
Disk thickness	0.008 m
Total area of undoped disks	0.66476 m^2
Total area of doped disks	329.7209 m^2
Area per stage	41.21512 m^2
Total reactor volume	14.8 L

Doping Process

Clay discs with a diameter of 0.23 m and a thickness of 0.008 m were used. As a first step, the discs were placed in a muffle furnace reaching 550 °C to eliminate organic matter residue.

The discs were impregnated with a solution of distilled water and zinc oxide. They were then calcined in a muffle furnace at 550 °C for one hour to improve the catalyst's adhesion to the clay surface.

The photo deposition technique was used for ZnO doping, using hydrated aluminum sulfate. A 15 L solution was prepared with a concentration of 300 ppm of Al+3. The disks were mounted on the reactor shaft, UV light lamps with a wavelength of 365 nm and 15 watts of power were turned on and

 doi:10.20944/preprints202410.0598.v1

allowed to irradiate for 4 h to photodope the disks with Al+3 particles, and then the disks were placed in the muffle at 550 °C for 1 h (Montalvo et al., 2018., He et al., 2015).

Catalyst Characterization Tests

SEM Tests

Scanning electron microscopy (SEM) is a technique by which it is possible to conclude whether the synthesis of the catalyst and the doping agent has been successful (Wang et al., 2018). A JEOL 7600F electron microscope operated at 10 kV was used for this. The elemental composition was determined utilizing the Oxford INCA X EDX bench, using the JEOL 7600F operated at 10 kV, and the samples were prepared on carbon tape.

This analysis provides information on the sample's composition by providing the percentages of the ZnO catalyst on the support and the presence of aluminum metal ions.

Diffuse Reflectance

To estimate the forbidden band width (Eg), the catalyst was analyzed utilizing a Thermo Scientific Evolution 600 UV spectroscopy equipped with an ISR-2200 integrating sphere. First, a magnesium oxide blank was analyzed, and then the samples were analyzed in the 200 to 800 nm range.

X-Rays

The photocatalyst was characterized by X-ray diffraction (XDR) to determine the chemical phases and crystallographic properties of the synthesized material (Rabiei et al., 2020); it was carried out using a Bruker D8 advanced X-ray diffractometer with a 1.54 A copper tube (35 Kv, 25 mA) as an X-ray source. The scanning was carried out between 10 and 70 (2 theta) with a step size of 0.03 / s.

To determine the synthesized material's chemical phases and crystallographic properties (Zyoud et al. 2015), in most processes, the effective use of nanocatalysts depends on the particle size and ease of manipulation. Therefore, it is of vital importance to characterize them using effective methods at low cost (Gupta et al., 2019).

Raman

RAMAN microscopy characterized the chemical structure of undoped and doped zinc oxide. This process was carried out on equipment that uses a 785 nm laser and a QE65000 Raman detector from Ocean Optics. A 785 nm infrared laser with a laser power of 75 mW was used for undoped ZnO oxide, but for doped ZnO, a laser power of 25 mW was used.

Preparation of Pyridine Solutions

1000 ppm pyridine stock solutions were prepared, and from these, different dissolutions were made with concentrations ranging from 10, 20, 30, 40, 60 to 80 ppm, handling the 14.8 L that is the total operating capacity of the photoreactor for each concentration handled.

The following relationship was used to find the relationship and prepare the solutions (10, 20, 30, 40, 60, and 80 ppm) of pyridine.

$C_1V_1=C_2V_2$

Degradation Tests

The degradation of pyridine was carried out for 72 h, with samples taken continuously every 6 h; the aliquot taken was approximately 5 mL in clean, dry, and labeled amber vials for later analysis in the UV-vis Carry 60 spectrometer and high-performance liquid chromatography (HPLC).

Initially, a pyridine sample was scanned to identify the maximum absorption peak and wavelength. Scans were performed on each sample taken from a wavelength of 200 to 500 nm. Likewise, HPLC analyzed each sample.

Gases Masses

 doi:10.20944/preprints202410.0598.v1

Gas chromatography-mass (GC-MS) is a technique that combines the separation capacity of gas chromatography with the sensitivity and selective capacity of the mass detector. This combination allows the analysis and quantification of trace compounds in complex mixtures with high effectiveness.

This technique is indicated for the separation of volatile and semi-volatile organic compounds. It consists of vaporizing the sample and injecting it into a capillary chromatographic column.

Elution occurs by the flow of a mobile phase of an inert gas that transports the analytes through the column. The analytes are retained reversibly because of a physical adsorption process. The separated components are eluted from the column and recorded by an MS detector, obtaining a mass spectrum representing the abundance of different types of ions based on the mass/charge ratio.

The use of GC-MS is restricted to separating compounds with a molecular weight of less than 1000 and a maximum working temperature of about 400ºC.

For this technique, an Agilent 6890N Network GC System gas chromatograph with an Agilent 5973 MSD mass detector (quadrupole), a DB5-MS column (30mx0.25mmx0.25µm), and a split/split less purge and trap injector (Teledyne Tekmar) were used.

For this, a temperature ramp that increased by 10 °C every minute until it reached 250 °C was used. This temperature was maintained for 3 minutes, then an increase of 10 °C was managed until it reached 355 °C and was maintained for 10 minutes. The ACQ method CIQ was used, which has already been established.

Results

Figure 2 shows the characterization of the catalysts synthesized by the SEM technique. In Figure 2 (A), a characteristic shape of undoped ZnO is observed with a crystal shape with an average size of 100 to 50 µm; a clean surface is observed. In Figure 2 (B), accumulations of small particles are observed on the surface of the ZnO, which are attributed to the deposited aluminum particles.

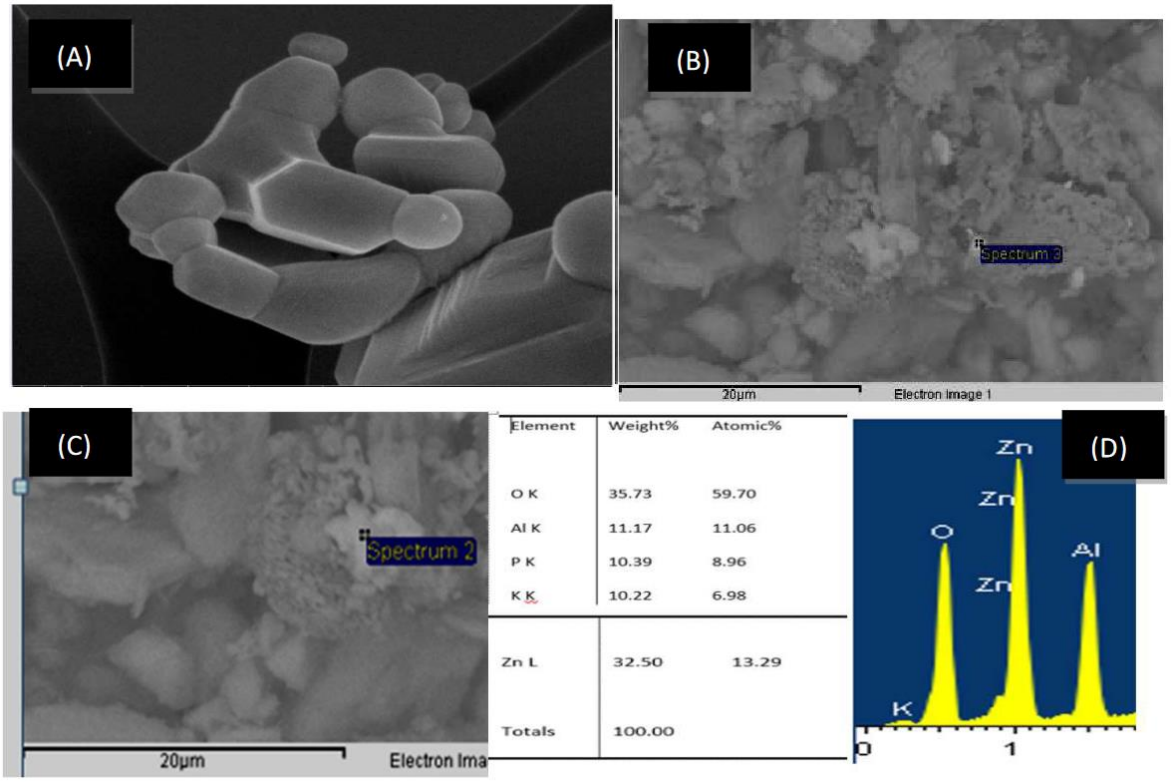

Figure 2. (A) Undoped zinc oxide, (B) Al^{+3} doped zinc oxide, (c) close-up of the doped area. EDS results of Al^{+3} doped zinc oxide.

Preprints.org (www.preprints.org) | NOT PEER-REVIEWED | Posted: 9 October 2024 doi:10.20944/preprints202410.0598.v1

The results of the SEM characterization and EDS analysis (Figure 2 (D)) show that Al^{+3} nanoparticles were indeed deposited on the surface of the zinc oxide. Although this is not a quantitative test but rather a qualitative one, the EDS result gives a percentage of 11% by weight of the doped material, and plasmons of this are shown in the microfilms presented (Figure 1 C).

X-Rays

An X-ray analysis of elemental compounds was carried out to verify that the aluminum was impregnated in the zinc oxide matrix.

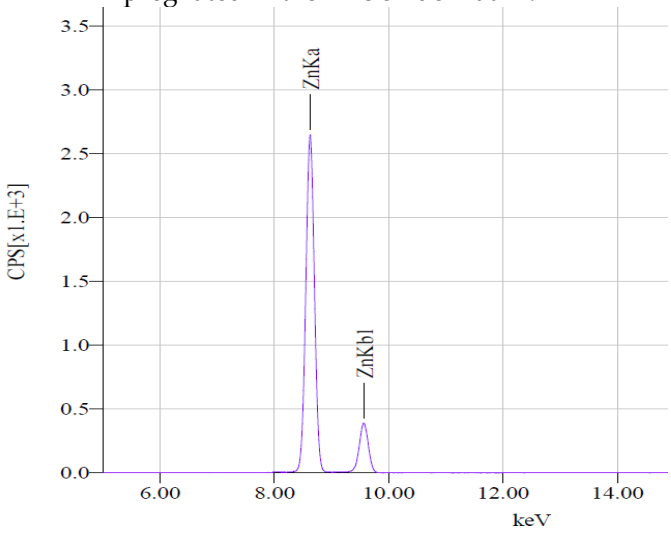

Quantitative result

Element	ms%	mol%
13 Al*	4.1077	9.4075
30 Zn*	95.8923	90.5925

Figure 3. Elemental compound X-ray analysis of the ZnO-Al^{+3} catalyst.

Aluminum is present at 4.1%, consistent with the mass concentration used in doping. This study confirms the presence of aluminum.

Diffuse Reflectance

The optical band gap can be estimated using the following Tauc relationship (Montalvo et al., 2018):

$\alpha h\nu = B(h\nu - Eg)^n$…..(9)

Where B is a constant and, Eg is the forbidden or optical bandwidth of the material, n is a number characterizing the nature of the electronic transition between the valence band and conduction band, which can have values 1/2, 2, 3/2, and 3 corresponding to the direct allowed, indirect allowed, direct forbidden, and indirect forbidden transitions, respectively.

It is well known that the direct transition through the forbidden band is feasible between the valence band and the conduction band bordering the "k-space." In the transition process, the total energy and momentum of the electron-photon system must be conserved.

It is known that ZnO is a direct band gap semiconductor, so from the above equation, it is clear that the graph of $(\alpha h\nu)^{1/2}$ vs. $h\nu$ will indicate a divergence at an energy value, for example, where the transition occurs. The value of the forbidden band depends on the nature of the transition (i.e., the n value) given.

The estimated band gap from the plot of $(\alpha h\nu)^{1/2}$ versus $h\nu$ for Al^{+3} doped ZnO particles can be seen in Figure 4. The band gap ("Eg") is determined by extrapolating the straight portion to the energy axis at $\alpha = 0$. The linear part shows that the transition mode in these particles is direct. The estimated band gap value of Al^{+3} doped ZnO was 3.08 eV. The band gap value is smaller than that of undoped ZnO of 3.37 eV; this might be due to the strain arising from the chemical synthesis of Al^{+3} doped ZnO. These microstrains greatly influence the optical band gap of the material (Raliya et al., 2017).

Preprints.org (www.preprints.org) | NOT PEER-REVIEWED | Posted: 9 October 2024 doi:10.20944/preprints202410.0598.v1

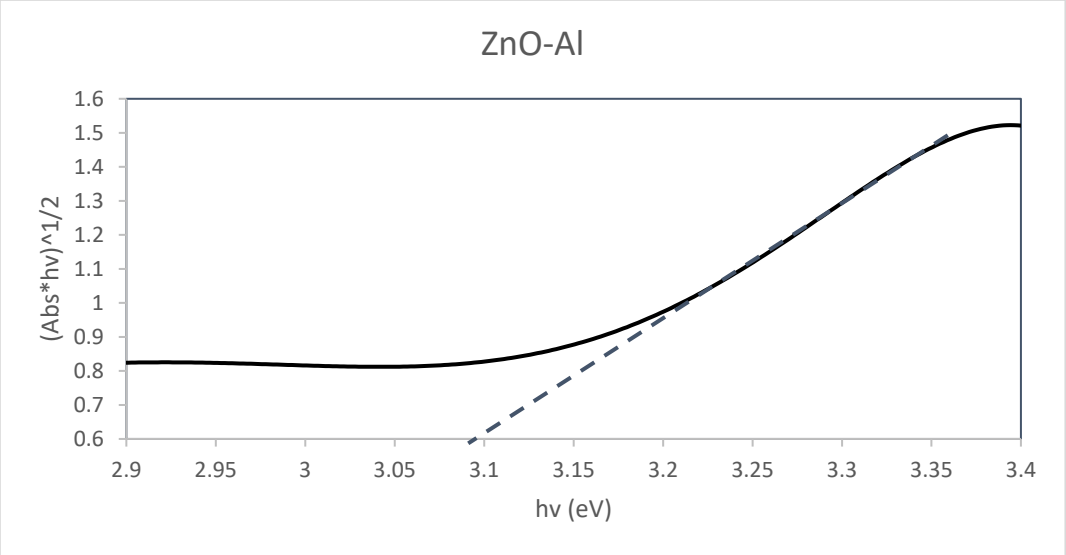

Figure 4. Plot showing $(\alpha h\nu)^{1/2}$ vs a hν for band gap determination of ZnO- Al material.

The transition mode in these ZnO nanoparticles was confirmed to be direct. The absorption coefficient near the band edge is also assumed to show an exponential dependence on photon energy, and this dependence is given as follows: (Salah et al., 2016, Wang et al., 2016).

$\alpha = \alpha_0 \exp(h\nu/E_u)$ ….. (10)

where α_0 is a constant, and E_u is the Urbach energy interpreted as the width of the tails of the localized states associated with the amorphous state in the forbidden gap.

Raman Spectroscopy

Figure 5 shows the Raman spectrum of undoped (red) and doped (blue line) ZnO. The first shows the characteristic peaks of zinc oxide. In this case, zinc oxide was obtained from its hexagonal phase (wursite), and its structure belongs to the C3v symmetry group in which the following vibration modes exist, determined by group theory, which is: $\Gamma = A_1 + 2B_1 + E_1 + 2E_2$.

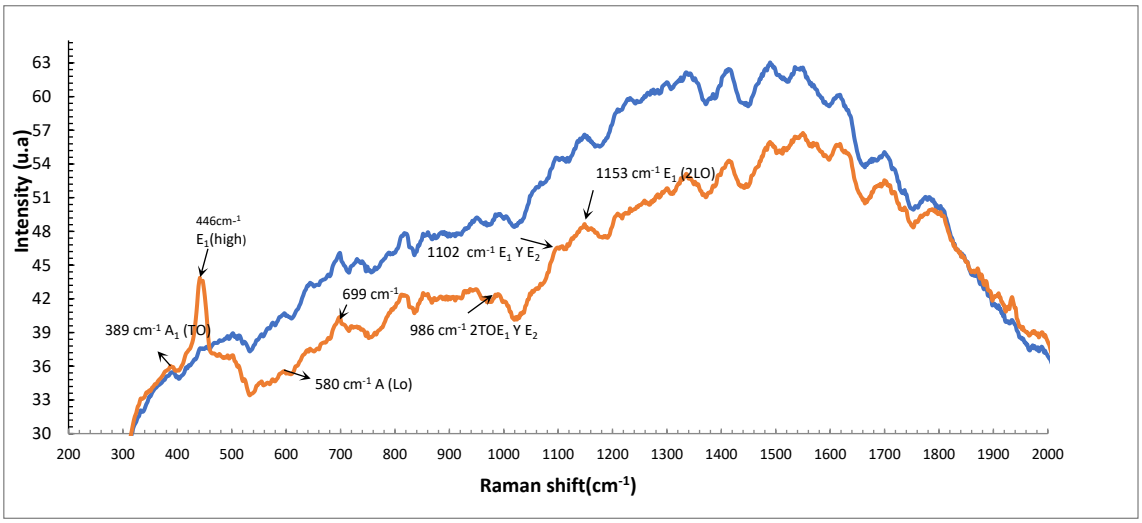

Figure 5. Raman spectrum of undoped ZnO and Al^{+3} doped ZnO.

The modes A_1, E_1, and E_2, E_2(low), E_2 (high)) are Raman active modes. The symmetrical modes A_1 and E_1 are Raman and Infrared active modes, E_2 is only Raman active and B1 is a forbidden mode for both Raman and Infrared. The polar characteristics of the A1 and E1 vibration modes lead to longitudinal and transverse components designated as A_1(TO), A1(LO), E_1(TO), and E_1(LO).

 doi:10.20944/preprints202410.0598.v1

Zinc oxide has a particular peak at 446 cm^{-1} that, when doped with Al^{+3} this peak is not observed and similar to the Raman spectrum of $ZnOAl^{+3}$ (doped), an increase in the intensity of the characteristic peaks 580 cm^{-1} A(Lo), 986 cm^{-1} E_1 and E_2, 1102 cm^{-1}. E1 and E_2 and 1153 cm^{-1} E_1 (2Lo) is seen; that is, there is an increase of 6 units of intensity on average in these peaks in the doped zinc oxide lines, which may be logical since the aluminum is on the surface of the zinc oxide and may be causing this.

Uv-Vis and HPLC Results

The UV-vis results are shown in Figure 6, which shows the characteristic peaks of pyridine at an initial time, peaks at 256 and 250 nm. Pyridine is a heterocyclic compound that presents several electronic transitions, which are combinations of the π-π^* y η-Π^* transitions, to which these characteristic peaks are attributed (Aguilar 2011, Medellín et al. 2013). The maximum peak decreases as the degradation time passes; in this case, the total exposure time was 72 h.

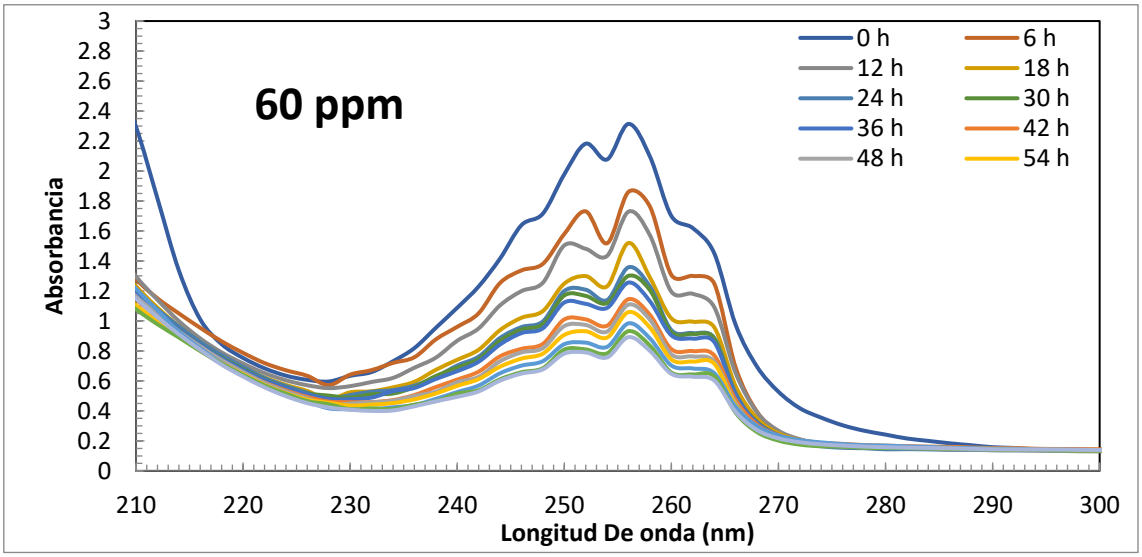

Figure 6. UV-vis spectrum of pyridine with an initial concentration of 60 ppm and 72 h of reaction using 15-watt natural light lamps, a rotation speed of 55 rpm, and using ZnO-Al as a catalyst.

During the first hours, the percentage of degradation between each 6 hours is approximately 39%. At the final times (48 to 72 h), this percentage is drastically reduced to 20%, with a photodegradation percentage of 62% after 72 h.

Figure 7 shows how the different initial concentrations used decrease over time. In the case of 60 and 80 ppm, after 24 hours, sufficient hydroxyl radicals were produced to attack the molecule. After 18 hours in the case of reaction, a 32% decrease is noted, and as time progresses up to 72 h, this decrease is constant but more minor. This may be due to the increase in intermediate compounds that are less susceptible to photooxidation.

 doi:10.20944/preprints202410.0598.v1

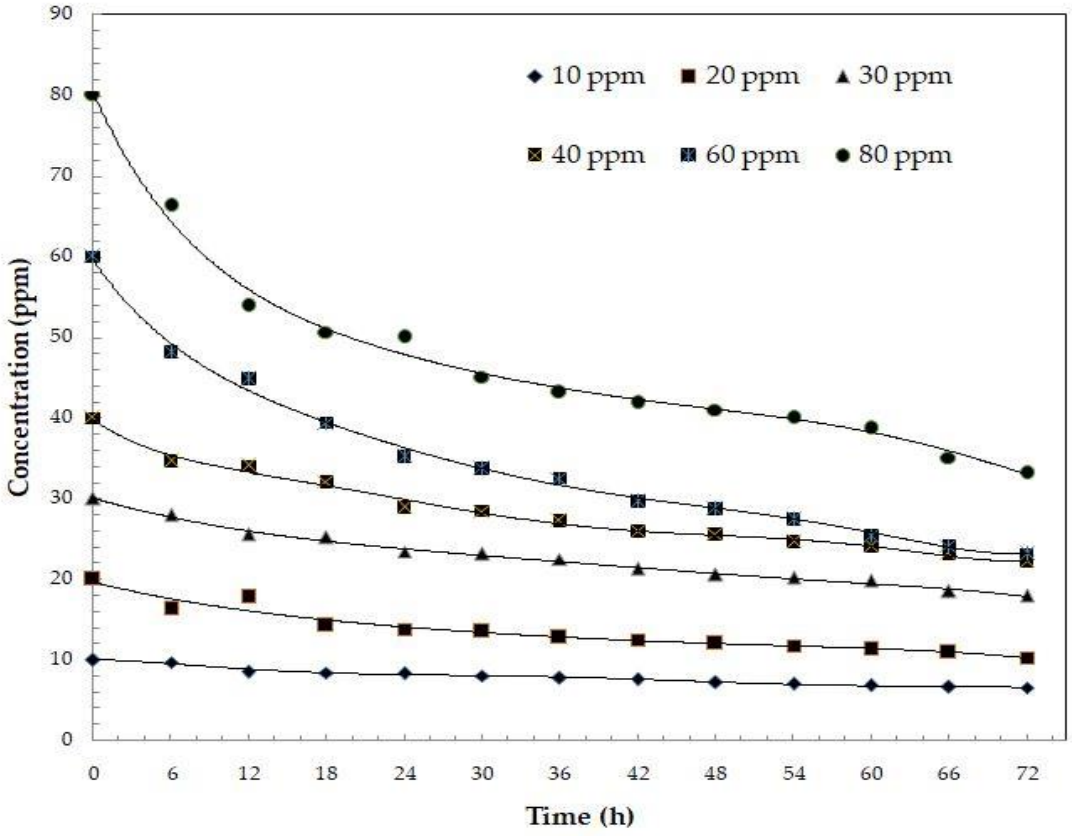

Figure 7. Graph of concentration vs degradation time of pyridine during 72 h of reaction using 15-watt natural light lamps, a rotation speed of 55 rpm, and using ZnO-Al as a catalyst.

Figure 8 shows the percentage degradation values determined using Equation 11.
% conversion = (1- Cf/Ci)*100…..(11)
Where: Cf = final concentration, Ci = initial concentration

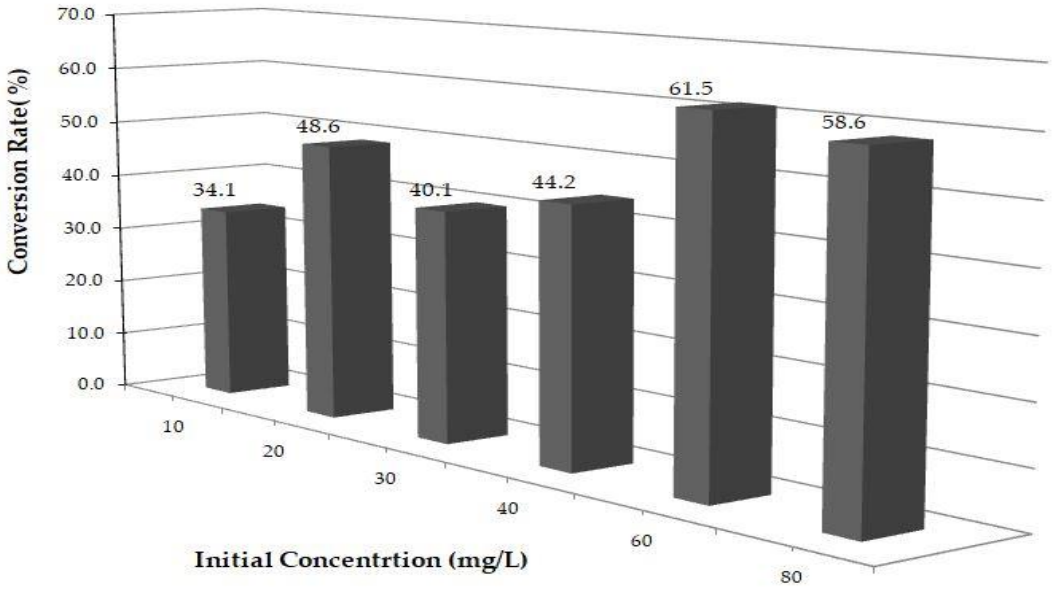

 doi:10.20944/preprints202410.0598.v1

Figure 8. Degradation percentages against initial concentration over a period of 72 h, using ZnO-Al with a rotation speed of 55 rpm and using natural light lamps.

Figure 8 shows that at low concentrations, the efficiencies are, on average, the same, 40% on average, which could be because when the concentration of the organic compound is low, the intermediate compounds are more abundant and more complex and can compete with the main molecule to be oxidized. While at high concentrations (60 and 80 ppm), the pyridine molecule is easily oxidized by the hydroxyl radicals formed, which monopolize most of it, considering that natural light is being used.

Kinetic Analysis

This indicates that photocatalytic oxidation reactions follow Langmuir-Hinshelwood-type kinetics (Fogler, 2001; Moctezuma et al., 2016; Mathews, 1992) as follows:

$$-r_a = -\frac{dC}{dt} = \frac{K_1 C}{1+K_2 C+\sum K_i C_i} \quad \text{.....(12)}$$

Where: K_1C represents the kinetic term of the rate equation, K_2C represents the adsorption term of the reactant, and $\sum(K_i C_i)$ represents the adsorption term of all the intermediate products of the degradation reaction of organic compounds.

If the experimental data are analyzed at very short reaction times, the adsorption term of the intermediate products can be neglected.

Based on the above, it can be shown that the following equation can represent the general kinetic form:

$$r_a = -\frac{dC}{dt} = \frac{K_1 C^m}{1+K_2 C^n} \quad \text{.....(13)}$$

If the exponents m and n have a value of 1, the constants K_1 and K_2 can be determined directly from the graph of reaction rate versus concentration.

Equation (13) can be linearized in the manner recommended by Fogler (2001) and Moctezuma et al. (2016), using the following initial conditions: t=0, C= C_0 and reaction rate, the following equations are obtained:

$$r_a|_{t=0} = \frac{K_1 C_0}{1+K_2 C_0} \text{.....(14)}$$

$$\frac{1}{-r_a|_{t=0}} = \frac{1+K_2 C_0}{K_1 C_0} = \frac{1}{K_1 C_0} = \frac{K_2 C_0}{K_1 C_0} \text{.....(15)}$$

$$\frac{1}{-r_a|_{t=0}} = \frac{1}{K_1 C_0} + \frac{K_2}{K_1} \text{.....(16)}$$

Equation (16) 's behavior is represented in Figure 9, where the ordinate at the origin is K_2/K_1, and the slope is given by $1/K_1$.

$$-r_{AC} = -\frac{dC_{AC}}{dt} = \frac{K_1 C_{AC}}{1+K_2 C_{AC}} \quad \text{.....(17)}$$

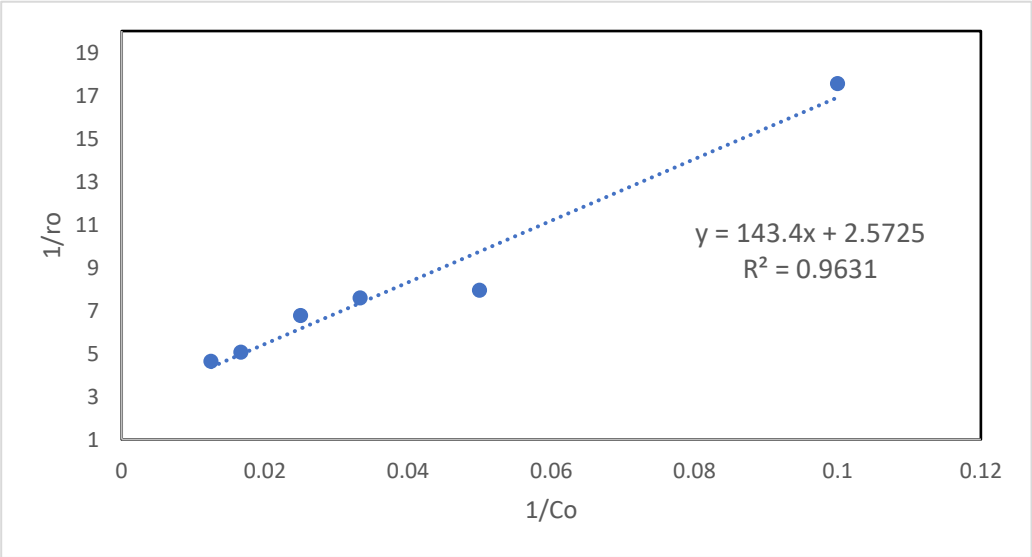

 doi:10.20944/preprints202410.0598.v1

Figure 9. Graph of 1/ro vs. 1/Co to obtain the K_1 and K_2 values of the LH-HW model.

From the values obtained in Figure 9, we have the values of the constants, and therefore, the previous equation is expressed as follows:

$$-r_{AC} = \frac{0.006973 * C_{PY}}{1 + 0.01794 * C_{PY}} \quad \text{.....(18)}$$

The values of the reaction constants K_1= 0.006973501 hr^{-1} and absorption K_2= 0.017939331 L/mg show that $k_2 > 2 * k_1$. Therefore, it can be said that the compound is absorbed on the surface, which helps to have closer contact with the hydroxyl radicals formed, which allows a better photodegradation of the compound.

Figure 10 shows the behavior of the LH-HW model of the experimental data and the model. The data is observed to have a behavior similar to the model, adjusting to its behavior.

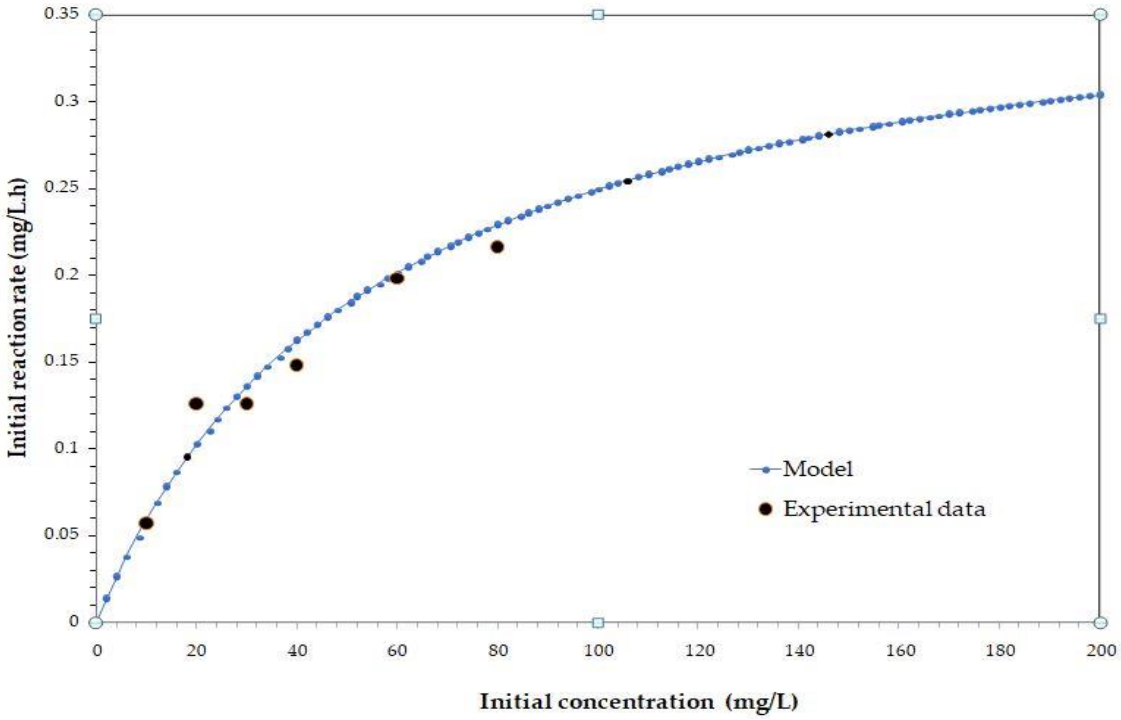

Figure 10. Initial reaction rate as a function of initial concentration (72 h of reaction using 15-watt natural light lamps, a rotation speed of 55 rpm, and using ZnO-Al as a catalyst).

Proposed Reaction Mechanism

The proposed mechanism for pyridine follows the formation pathway of 2-hydroxy pyridine until the double bonds are weakened and the ring cycle of this compound is broken. It can be assumed that carboxylic acids and other acids are formed.

The experimental results show the formation of 2-hydroxypyridine in the first instance. Inspection of the charged resonance forms suggests that the electron density on the alpha and gamma carbon atoms is especially low; consequently, a beta substitution should be expected, also because this position is the only one in which the transition state in the substitution does not have a resonance form with a charge on the trivalent nitrogen.

Once 2-hydroxy pyridine is formed, it can lead to the formation of 2,3-dihydropyridine, but according to the results of the gas-mass study, 2,6-dihydropyridine is formed. This weakens the benzene ring, leading to the weakening of the carbon-nitrogen bond, thus forming the monoamine of 3-pentanoic acid or 3-amino pentanoic acid. (3-amino pentanoic acid)

Many agree that the next step is the formation of succinic acid or, where appropriate, glutamic acid before it breaks down into carboxylic acid compounds or other derivatives.

 doi:10.20944/preprints202410.0598.v1

Subsequently, the formation of the compound acetic acid, butyl ester, and 2-butoxy ethanol is observed.

The proposed mechanism is shown in Figure 11, supported by the mass gas analyses.

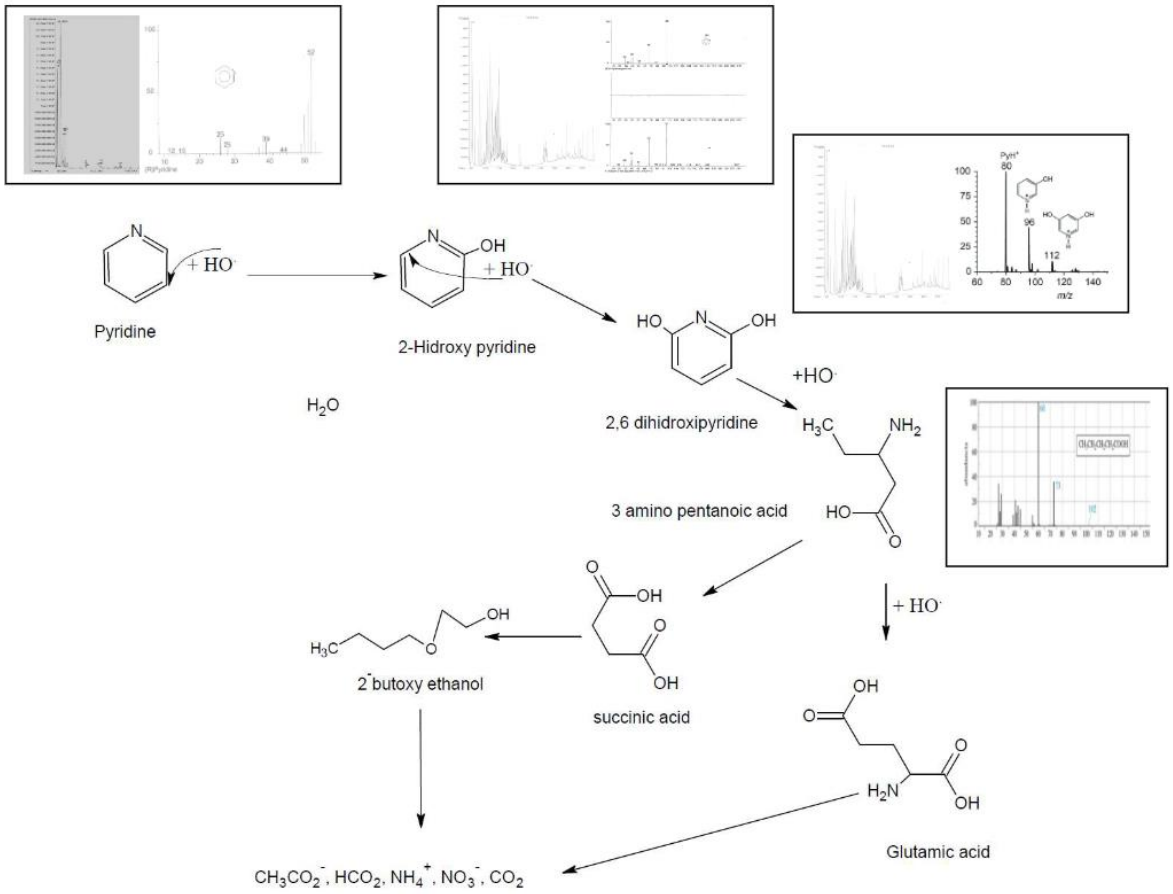

Figure 11. Proposed reaction mechanism for the degradation of Pyridine in a rotating photonic reactor in a reaction time of 72 h using 15-watt natural light lamps, a rotation speed of 55 rpm, and using ZnO-Al as a catalyst.

References

1. Aguilar, C. A., Montalvo, C., Ceron, J.G. and Moctezuma, E. (2011). Photocatalytic Degradation of Acetaminophen.Int. J. Environ. Res., 5(4):1071-1078.
2. Aguilar, U. C., Anguebes F. F., Cerón B. J., Cerón B. R., Córdova Q. A., Montalvo. R. C., Rangel M. M., Zavala L. J. (2012). Tópicos Selectos de Ingeniería Química. ISBN: 978-607-7826-25-5. Primera edición. Cap. 4 (75-89).
3. Bello, M. M., & Raman, A. A. A. (2018). Adsorption and Oxidation Techniques to Remove Organic Pollutants from Water. En: Green Adsorbents for Pollutant Removal (Malaya, Kuala Lumpur, Malaysia), pp. 249-300. https://www.researchgate.net/publication/326012580_Adsorption_and_Oxidation_Techniques_to_Remove_Organic_Pollutants_from_Water.
4. Bozena Czech, Katarzyna Rubinowska (2013). TiO2-assisted photocatalytic degradation of diclofenac, metoprolol, estrone and chloramphenicol as endocrine disruptors in water. University of Life Sciences in Lublin, Adsorption 19:619–630. [11]
5. Careghini, A., Mastorgio, AF, Saponaro, S. & Sezenna, E. (2015). Bisphenol A, nonylphenols, benzophenones, and benzotriazoles in soils, groundwater, surface water, sediments, and food: a review. Environmental Science and Pollution Research. Vol. 22. 5711-5741. https://link.springer.com/article/10.1007%2Fs11356-014-3974-5.
6. El Nemr, A., Helmy, E. T., Gomaa, E. A., Eldafrawy, S., & Mousa, M. (2019). Photocatalytic and Biological Activities of Undoped and Doped TiO2 Prepared by Green Method for Water Treatment. Journal of Environmental Chemical Engineering. Vol. 7(5). 103-385. https://www.sciencedirect.com/science/article/abs/pii/S2213343719305081.

 doi:10.20944/preprints202410.0598.v1

7. Elsayed M. A. (2013). Successive advanced oxidation of pyridine by ultrasonic irradiation:effect of additives and kinetic study. Desalination and Water Treatment,vol 1 pag 1-9 doi: 10.1080/19443994.2013.837003
8. Fogler, H.S. Elements of Chemical Reaction Engineering. Prentice Hall, N.J., 2021
9. Frolov, N.A., Vereshchagin, A.N. (2023). Piperidine Derivatives: Recent Advances in Synthesis and Pharmacological Applications. Int. J. Mol. Sci. 2023, 24, 2937. https:// doi.org/10.3390/ijms24032937
10. Grigor'eva Nellya G., Filippova Nadezhda A.,Tselyutina Marina I., Kutepov Boris I. (2015) Synthesis of pyridine and methylpyridines over zeolite catalysts. Appl Petrochem Res., 5: 99–104
11. 28Gupta, N., O'Loughlin, E. J., & Sims, G. K. (2019). Microbial Degradation of Pyridine and Pyridine Derivatives. Microbial Metabolism of Xenobiotic Compounds, 1–31.
12. He, B., Zhao, Q., Zeng, Z., Wang, X. & Han, S. (2015). Effect of hydrothermal reaction time and calcination temperature on properties of Au@CeO2 core–shell catalyst for CO oxidation at low temperature. Journal of Materials Science 50(19), 6339–6348. https://link.springer.com/article/10.1007/s10853-015-9181-z.
13. Islam, M. T., Jing, H., Yang, T., Zubia, E., Goos, A. G., Bernal, R. A., Botez, C. E., Narayan, M., Chan, C. K. & Noveron, J. C. (2018). Fullerene Stabilized Gold Nanoparticle Supported on Titanium Dioxide for Enhanced Photocatalytic Degradation of Methyl Orange and Catalytic Reduction of 4-nitrophenol. Journal of Environmental Chemical Engineering 6(4), 3827-3836. https://www.sciencedirect.com/science/article/abs/pii/S221334371830277X.
14. Kaur, A., Gupta, G., Ibhadon, A. O., Salunke, D. B., Sinhad, A.S.K. & Kansala, S. K. (2017). A Facile synthesis of silver modified ZnO nanoplates for efficient removal of ofloxacin drug in aqueous phase under solar irradiation. Journal of Environmental Chemical Engineering 6(3), 3621-3630. https://www.sciencedirect.com/science/article/abs/pii/S2213343717302233.
15. Koe, W. S., Lee, J. W., Chong, W. C., Pang, Y. L. & Sim, L. C. (2020). An overview of photocatalytic degradation: photocatalysts, mechanisms, and development of photocatalytic membrane. Environmental Science and Pollution Research 27, 2522-2565. https://link.springer.com/article/10.1007/s11356-019-07193-5.
16. Matthews, Ralph W and McEvoy Stephen R. (1992) Photocatalytic degradation of phenol in the presence of near-UV illuminated titanium dioxide. Journal of Photochemistry and Photobiology A: Chemistry. Volume 64, Issue 2, 231-246, https://doi.org/10.1016/1010-6030(92)85110-G.
17. Marinescu, M; Popa, C. (2022). Pyridine Compounds with Antimicrobial and Antiviral Activities. Int. J. Mol. Sci. 2022, 23(10), 5659; https://doi.org/10.3390/ijms23105659
18. Medellin C. N., Ocampo R., Leyva R. R., Sanchez P. M., Rivera U. J., Méndez D. J. (2013).Removal of diethyl phthalate from water solution by adsorption, photo-oxidation, ozonation and advanced oxidation process (UV/H2O2, O3/H2O2 and O3/activated carbon). Science of The Total Environment. 442., 1: 26-35. https://doi.org/10.1016/j.scitotenv.2012.10.062
19. Moctezuma E., López M., Zermeño B. (2016). Reaction pathways for the photocatalytic degradation of phenol under different experimental conditions. Revista Mexicana de Ingeniería Química. 15: 1, 129-137.
20. Mohammed M. Rahman, SherBahadarKhan, Abdullah M. Asiri, Khalid A. Alamry, AftabAslamParwazKhan, AnishKhan, Malik Abdul Rub, NavedAzum. (2013) Acetone sensor based on solvothermally prepared ZnO doped with Co3O4nanorods. Microchim.ActaVolumen 180, pp 675-685.
21. Montalvo, C., Aguilar, C., Alcocer, R., Ramirez, M., & Cordova, V. (2018). A Semi-Pilot Photocatalytic Rotating Reactor (RFR) with Supported TiO2/Ag Catalysts for Water Treatment. Molecules 23(1), 224. https://www.ncbi.nlm.nih.gov/pmc/articles/PMC6017124/.
22. Raliya, R., Avery, C., Chakrabarti, S., & Biswas, P. (2017). Photocatalytic degradation of methyl orange dye by pristine titanium dioxide, zinc oxide, and graphene oxide nanostructures and their composites under visible light irradiation. Applied Nanoscience, 7, 253-259.
23. Rabiei Marzieh, Palevicius Arvydas, Monshi Ahmad, Nasiri Sohrab, Vilkauskas Andrius and Janusas Giedrius. (2020). Comparing Methods for Calculating Nano Crystal Size of Natural Hydroxyapatite Using X-Ray Diffraction Nanomaterials , 10(9), 1627; https://doi.org/10.3390/nano10091627
24. Salah, N., Hameed, A., Aslam, M., Babkair, S. S., Bahabri, F.S. (2016). Photocatalytic activity of V doped ZnO nanoparticles thin films for the removal of 2- chlorophenol from the aquatic environment under natural sunlight exposure. Journal of Environmental Management, 177, 53-64.
25. Santhi, K., Manikandan, P. & Rani, C. (2015). Synthesis of nanocrystalline titanium dioxide for photodegradation treatment of remazol brown dye. Appl Nanosci 5, 373-378. https://link.springer.com/article/10.1007/s13204-014-0327-0.
26. Song KeKe, Chen Jian, Song Yun. (2021). The degradation of pyridine wastewater by ozonation catalyzed by calcined zinc-magnesium-aluminum hydrotalcites[J]. Journal of Beijing University of Chemical Technology, 48(2): 8-15 . https://doi.org/10.13543/j.bhxbzr.2021.02.002.
27. Swarnakar P., Kanel S., Nepal D., Jiang Y., Jia H., KerrL., Goltz M., Levy J., Rakovan J. (2013). Silver deposited titanium dioxide thin film for photocatalysis of organic compounds using natural light. Solar Energy 88:242-249. 10.1016/j.solener.2012.10.014

 doi:10.20944/preprints202410.0598.v1

28. Wang, Z., Luo, C., Zhang, Y., Gong, Y., Wu, J., Fu, Q. & Pan, C. (2018). Construction of hierarchical TiO2 nanorod array/graphene/ZnO nanocomposites for high-performance photocatalysis. Journal of Materials Science, 53 (22), 15376–15389.
29. Wang, L., Liu, S., Wang, Z., Zhou, Y., Qin, Y., & Wang, Z. L. (2016). Piezotronic Effect Enhanced Photocatalysis in Strained Anisotropic ZnO/TiO2 Nanoplatelets via Thermal Stress. American Chemical Society Nano, 10, 2636-2643.
30. Zyoud, A., Zu'bi, A., Helal, M. H. S., Park, D., Campet, G. & Hilal, H. S. (2015). Optimizing photo-mineralization of aqueous methyl orange by nano-ZnO catalyst under simulated natural conditions. Journal of Environmental Health Science and Engineering, 13 (1), 46.
31. Zhang, Y., Jiang, W., Ren, Y., Wang, B., Liu, Y., Hua, Q. & Tang, J. (2020). Efficient photocatalytic degradation of 2-chloro-4,6-dinitroresorcinol in salty industrial wastewater using glass-supported TiO2. Korean Journal of Chemical Engineering 37(3), 536–545. https://link.springer.com/article/10.1007/s11814-019-0448-y.
32. Zhu, C., Yue, H., Jia, J., and Rueping, M. (2020).Recent advances in nickel-catalyzed C-heteroatom cross-coupling reactions under mild conditions via facilitated reductive elimination Angew. Chem. Int. Ed. Vol 60(33). 17810-17831.
33. Anwer, H., Mahmood, A., Lee, J., Kim K., Park J., Yip A. (2019). Photocatalysts for degradation of dyes in industrial effluents: Opportunities and challenges. Nano Res. Vol. 12. 955–972. https://doi.org/10.1007/s12274-019-2287-0
34. Badvi, K y Javanbakht, V. (2021). Enhanced photocatalytic degradation of dye contaminants with TiO2 immobilized on ZSM-5 zeolite modified with nickel nanoparticles. Journal of Cleaner Production 280(2), 124518. https://www.sciencedirect.com/science/article/abs/pii/S0959652620345625.
35. Ashok K., Suraj K., Sabnaz K., Nandan S., Subhasis B. and Sanjay D. (2022). Pyridine: the scaffolds with significant clinical diversity Sourav D., RSC Adv., 12, 15385.
36. Hasan, A. K. M. M., Dey, S. C., Rahman, M. M., Zakaria, A. M., Sarker, M., Ashaduzzaman, M.D. & Shamsuddin, S. M. D. (2020). A kaolinite/TiO2/ZnO-based novel ternary composite for photocatalytic degradation of anionic azo dyes. Bulletin of Materials Science 43(1), 27. https://link.springer.com/article/10.1007/s12034-019-1964-4.